Journal of Materials Chemistry A

Accepted Manuscript

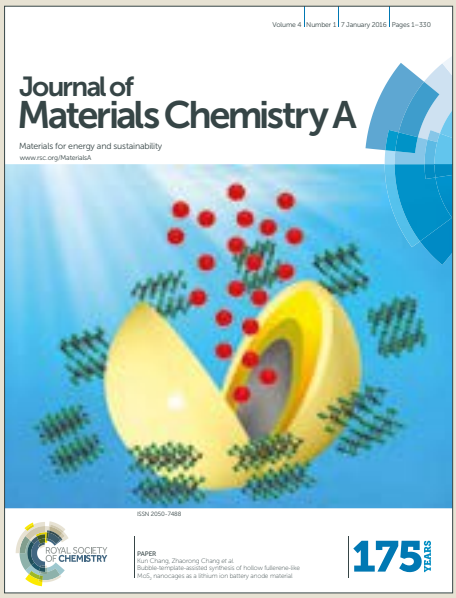

ROYAL SOCIETY OF CHEMISTRY

rsc.li/materials-a

View Article Online
DOI: 10.1039/C8TA06296J

Mitigating Oxygen Release in Anionic-Redox-Active Cathode Materials by Cationic Substitution through Rational Design

Thomas A. Wynn[a], Chengcheng Fang[a], Minghao Zhang[b], Haodong Liu[b], Daniel M. Davies[b], Xuefeng Wang[b], Derek Lau[b], Jungwoo Z. Lee[b], Bo-Yuan Huang[c], Kuan-Zong Fung[c], Chung-Ta Ni[c], Ying Shirley Meng[a,b,d]*

a. Materials Science and Engineering Program, University of California San Diego, La Jolla, CA 92093, USA

b. Department of Nanoengineering, University of California San Diego, La Jolla, CA 92093, USA

c. Department of Materials Science and Engineering, National Cheng Kung University, Tainan 70101, Taiwan, ROC

d. Sustainable Power and Energy Center, University of California San Diego, La Jolla, CA 92093, USA

*e-mail: shirleymeng@ucsd.edu

Density functional theory is coupled with experiment to explore the ability of substitutional doping to reduce oxygen vacancy formation energy in Li-rich layered oxide bulk, showing improved oxygen stability with Mo and Ru incorporation.

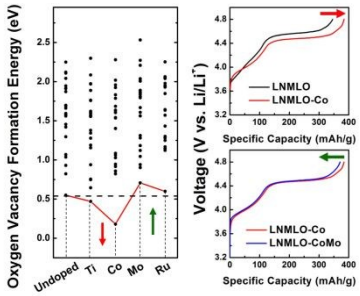

ROYAL SOCIETY OF CHEMISTRY View Article Online
DOI: 10.1039/C8TA06296J

Journal of Materials Chemistry A

ARTICLE

Mitigating Oxygen Release in Anionic-Redox-Active Cathode Materials by Cationic Substitution through Rational Design

Received 00th January 20xx,
Accepted 00th January 20xx

DOI: 10.1039/x0xx00000x

www.rsc.org/

Thomas A. Wynn,‡[a] Chengcheng Fang,‡[a] Minghao Zhang,[b] Haodong Liu,[b] Daniel M. Davies,[b] Xuefeng Wang,[b] Derek Lau,[b] Jungwoo Z. Lee,[b] Bo-Yuan Huang,[c] Kuan-Zong Fung,[c] Chung-Ta Ni,[c] and Ying Shirley Meng *[a,b,d]

When substituting excess lithium in the transition metal layer, oxygen extends its role as a framework in classical layered oxide cathodes, exhibiting electrochemical activity and enhancing the reversible capacities of layered oxides through anionic redox mechanisms. Though oxygen activity comes with instability in the form of oxygen loss, which is associated with irreversible voltage decay and capacity fade. To understand this irreversible loss and to increase the stability of lattice oxygen, density functional theory is applied to calculate oxygen vacancy formation energies in lithium rich transition metal layered oxides for a variety of dopants, noting increased stability upon doping with 4d elements Mo and Ru. Driven by these findings, Mo is co-doped with Co into $Li[Li_{0.2}Ni_{0.2}Mn_{0.6}]O_2$, showing notably reduced voltage decay and capacity fade without sacrificing energy density and cycle life, and evidence of Mo incorporation is presented. Calculations suggest this is due to a modified charge density distribution around anions upon incorporation of Mo, altering local band structure and impeding oxygen vacancy formation, while maintaining the anionic activity available for redox.

Introduction

Lithium ion battery technology has enabled the advancement of handheld devices and electric vehicles, and has reached to grid-scale storage markets. To further these technologies, improving battery life and extending electric vehicle ranges, the energy density of LIB cathodes must increase well beyond the current reach of commercially available cathodes.[1,2] Lithium rich layered oxide cathodes have sparked intense interest due to their strikingly high capacities, in excess of 250 mAh/g—well beyond the capacity of current commercial cathodes such as $LiCoO_2$, $LiMn_2O_4$ and $LiFePO_4$ (160, 120, and 168 mAh/g, respectively).[3] This is generally attributed to anionic redox behaviour—a phenomenon under intense scrutiny, yet widely accepted as the source of this capacity.[4–6] Unfortunately, the increased capacity is accompanied by a host of issues, including sensitivity to processing method,[7] transition metal (TM) migration,[8] surface phase transformations,[9] and the irreversible release of oxygen.[10–12] Further, this oxygen loss subsequently reduces the barrier for transition metal migration.[13] A combination of these effects leads to characteristic voltage decay and capacity fade. Many methods have been employed to combat this rapid degradation, including surface modification[14,15] and coating,[16] morphological control,[17] and incorporation of dopants;[18] each method shows a degree of improvement in one aspect of cycling, yet a comprehensive solution to Li-rich layered oxide cathodes shortcomings is still lacking. Despite the clear role of surface phase evolution in lithium rich layered oxide cathodes, the majority of oxygen activity occurs in the bulk, and doping remains an effective strategy for modifying bulk properties.

Most recent computational advances have described the notion of anionic redox in terms of two general phenomena: reorientation of oxygen ions into peroxo-like oxygen dimers, in the case of 4d transition metal layered oxides,[4,19] and more relevant to 3d transition metal elements, the alignment of two lithium ions across an oxygen atom creating labile oxygen states, susceptible to redox.[20] With respect to doping in particular, an extensive amount of *ab initio* calculations and experiments have been performed in Li-rich layered oxide cathodes. Computationally, density functional theory (DFT) studies generally provide insight into structural modification, band structure, voltage, and diffusion behaviour. Though the majority of these studies lack experimental interpretation, and, similarly, if experimental doping studies exist, these experiments lack description in terms of this computational work. A few noteworthy exemptions include the work of Deng et al.,[18] Wang et al.,[21] Xiao et al.,[22] and Gao et al.[23] Deng et al.[18] and Wang et al.[21] performed a range of cationic substitution experiments on lithium-rich NiMn layered oxides for a range of TM stoichiometries; results showed an increased initial charging plateau for the Co substitution and decreased plateau for the Ti

[a] Materials Science and Engineering Program, University of California San Diego, La Jolla, CA 92093, USA
[b] Department of Nanoengineering, University of California San Diego, La Jolla, CA 92093, USA
[c] Department of Materials Science and Engineering, National Cheng Kung University, Tainan 70101, Taiwan, ROC
[d] Sustainable Power and Energy Center, University of California San Diego, La Jolla, CA 92093, USA

†Electronic Supplementary Information (ESI) available: See DOI: 10.1039/x0xx00000x

‡ These authors contributed equally.

substitution, attributed to the degree of overlap between the dopant t_{2g} and O 2p orbitals, correlated to the extent of electron localization.[18] This work was followed up by a computational explanation of the impact of cation substitution on oxygen evolution, attributing increased oxygen loss to an effective decrease in band gap. The band gap is viewed as an impediment to charge transfer, a prerequisite for oxygen evolution.[22] Gao et al.[23] and Kong et al.[24] have performed the most comprehensive computational screening, both applied to Li_2MnO_3, Kong performing a comparative study between the classical layered and Li-rich analogue. Gao et al.[23] calculate oxygen release energies by removing anions with the lowest Bader charge on delithiation, predicting Nb-doping as a stabilizing agent, and Kong et al.[24] shows that typical dopants are thermodynamically stable within the Li-rich layered oxide framework and have the potential to alter electronic conductivity through hole polaron formation. Prior to this work, Gao et al.[25] had also calculated the impact of doping Mo into Li_2MnO_3, predicting a reduced band gap and improved Li mobility between Li and TM layers. Aforementioned doping experiments are generally difficult to describe via computation due to the potential for effects beyond purely bulk doping; as such, low doping amounts are used in this study to aid ease of dopant incorporation and prevent notable surface effects. Other experimental doping includes Ba into Li-rich NiMn layered oxide (LNMLO) cathode, showing improved rate capability[26] and B-doping into Li-rich NiMnCo showing modified crystallization[27] and improved oxygen redox reversibility[28], not calculated in this study due to interstitial incorporation rather than substitution. A multitude of other doping studies generally show that substitution of a small percentage of metal cations significantly alters cathode performance, though most experimental studies generally lack experimental evidence of incorporation and further lack the theoretical framework to understand the role of the dopant in these changes. Moreover, the importance of local environment to the dopant is not addressed in most computational work.

This work uniquely combines *ab initio* calculations of oxygen stability in LNMLO cathode material with experimental synthesis and characterization based on these findings, focusing on the notion of site-dependent anion stabilization in the lithium rich layered oxides. Analysis of the delithiated structure, subsequent structural changes, and bonding environment changes increase the complexity of the model, more closely resembling the true nature of an experimental material. Using first principles approaches, we show that oxygen vacancy formation is highly dependent on the local bonding environment, which has been shown to vary with the state of charge of the cathode. Using this site-based approach, we relate oxygen stability to the local environment changes during cycling. Findings of formation energies are rationalized using calculated data, showing a strong influence of doping on the charge density distribution, affecting the potential to form of oxygen vacancies. Doping of LNMLO with Al, Ti, Co, and Mo is then performed, clearly impacting the initial charging plateau associated with oxygen redox and loss. Al and Ti doping show little change to the oxygen redox plateau, as predicted by computation of the E_{Ov}^{F} calculations. Co-doping shows the opposite effect, due to increased oxygen loss from the lattice, again as predicted. When co-doped with Co and Mo, reduced oxygen loss, reduced voltage fade and improved capacity retention are observed. Incorporation of the Mo dopant is evident through X-ray diffraction, X-ray photoemission spectroscopy and energy dispersive X-ray spectroscopy. These findings demonstrate that *ab initio* calculations can be used to rationally select cation dopants to improve oxygen stability within the bulk of lithium rich layered cathode materials, while leaving oxygen available for reversible redox.

Experimental

Density Functional Theory

A spin-polarized GGA+U approximation to the Density Functional Theory (DFT) was employed, to account for electron correlations in transition metal and rare earth elements. Projector augmented-wave method (PAW) pseudopotentials were used as implemented in the Vienna Ab initio Simulation Package (VASP). The Perdew-Burke-Ernzerhof exchange correlation and a plane wave representation for the wavefunction with a cut-off energy of 450 eV were used. The Brillouin zone was sampled with a k-points mesh of 5 x 4 x 7 for structural relaxations and oxygen vacancy formation energy calculations and 10 x 8 x 14 for density of states (DOS) calculations, both by Gamma packing. Atomic coordinates and lattice vectors were fully relaxed for each structure. Effective U values used in the calculations are provided in the Supplemental Information, applied with the rotationally invariant approach.[29]

Cathode Synthesis

Pristine $Li[Li_{0.2}Ni_{0.2}Mn_{0.6}]O_2$ (LNMLO), Co-doped $Li[Li_{0.144}Ni_{0.136}Co_{0.136}Mn_{0.544}]O_2$ (LNMLO-Co), and Mo-co-doped $Li[Li_{0.144}Ni_{0.136}Co_{0.136}Mn_{0.544}]_{0.99}Mo_{0.01}O_2$ (LNMLO-CoMo) materials were synthesized by carbonate co-precipitation method (CCP). TM nitrate solutions (Ni:Mn = 1:3, Ni:Co:Mn = 1:1:4, 1M) were titrated into $NaCO_3$ solution (0.2 M) under stirring. The pH value during the co-precipitation process was carefully controlled between 7.80 and 7.85 to avoid hydroxide precursor generation. The slurry was then aged at 80 °C for 12 hours. After washing and drying, the TM carbonate precursor was sufficiently mixed with a stoichiometric amount of Li_2CO_3 and MoO_2. The two-step calcination conditions are 500 °C for 5 hours and 850 °C for 15 hours.

View Article Online
DOI: 10.1039/C8TA06296J

X-ray diffraction

X-ray powder diffraction (XRD) spectra were acquired using a Bruker D8 Advance diffractometer with a Bragg-Brentano θ-2θ geometry and a Cu Kα source (λ = 1.54 Å). Samples were scanned from 10° to 80° at a scan rate of 0.05°/step. Rietveld refinement was performed using FullProf software.

Electron microscopy

High-angle annular dark-field (HAADF) imaging was carried out on a Cs-corrected FEI Titan 300 kV transmission electron microscope (TEM)/scanning transmission electron microscope (STEM). All HAADF images were acquired at 300 kV and with a beam size of ~0.7 Å. To minimize possible electron beam irradiation effects, HAADF images were acquired from areas without pre-beam irradiation. STEM/energy dispersive spectroscopy (EDS) was performed on primary particles using a JEOL JEM-2800 at 200 kV in ADF mode. Scanning electron microscopy (SEM)/EDS spectra were collected from focused ion beam (FIB) cross-sections of pristine secondary particles. FIB cross-sections were prepared using an FEI Scios™ Dualbeam™ FIB.

X-ray photoelectron spectroscopy

X-ray photoelectron spectroscopy (XPS) was performed using a Kratos AXIS Supra with the Al anode source operated at 15 kV. The chamber pressure was < 10^{-8} Torr during all measurements. High-resolution spectra were calibrated using the hydrocarbon C1s peak at 284.6 eV. Data fitting was performed using CasaXPS software using a Shirley-type background.

Electrochemical Measurement

Cathodes consisting of 80 wt % of active materials, 10 wt % of Super P carbon, and 10 wt % of poly(vinylidene fluoride) (PVDF) binder were assembled into standard 2016 coin cells with Li metal as the anode and 1 M $LiPF_6$ in ethylene carbonate/dimethyl carbonate (EC:DMC in 3:7 weight ratio) as the electrolyte. The electrodes were assembled in a R2016 coin cells, where the active materials are the working electrodes and Li metal serves as the counter electrode. The mass loading is ~ 3 mg/cm^2. Electrochemical performance was measured using an Arbin battery cycler in galvanostatic mode between 2.0 – 4.8 V vs. Li/Li$^+$, at a current density of 12.5 mA/g for the first cycle and 25 mA/g for following cycles. The plateau length refers to the capacity above 4.4 V after normalizing the plateau voltage of doped materials to that of pristine materials. Electrochemical impedance spectroscopy (EIS) measurements were carried out using a Solatron 1287 potentiostat, with a 10 mV perturbation and AC frequencies from 0.01 to 1 × 10^6 Hz on as assembled electrodes and after 30 cycles. An equivalent circuit model was fit to the data to analyse the reactions that took place using Z view software (v. 3.4a, Scribner Associates, Inc.).

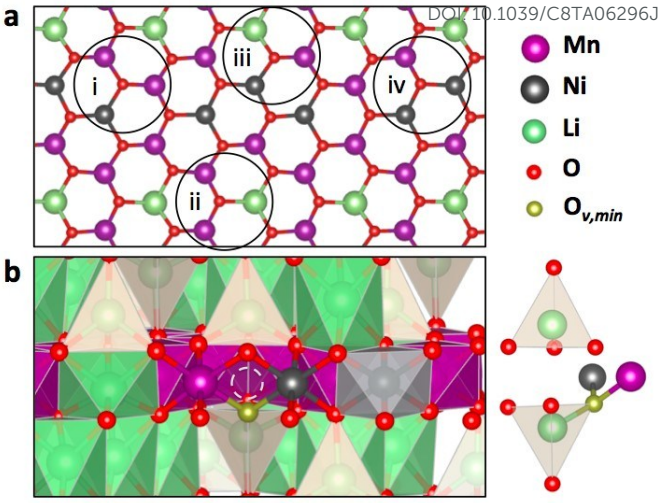

Figure 1: (a) The undoped structural model used in this study contains four general TM environments for each oxygen atom: (i) Mn-Mn-Ni, (ii) Mn-Mn-Li, (iii) Mn-Ni-Li, and (iv) Mn-Ni-Ni; (b) Relaxed structure contains a wider range of neighbouring configurations, including the formation of lithium dumbbells, isolated at right, around lithium vacancies within the transition metal layer (dashed circle).

Oxygen Vacancy Formation Energy

A model supercell was used containing 14 Li (2 within the transition metal layer), 3 Ni, 7 Mn and 24 O, corresponding to a stoichiometry of $Li[Li_{2/12}Ni_{3/12}Mn_{7/12}]O_2$. In this manuscript, the fully lithiated state is referred to as "pristine", and the material lacking dopants as "undoped". For doping studies, one dopant ion, M, is substituted for Mn, resulting in a stoichiometry of $Li[Li_{2/12}Ni_{3/12}Mn_{6/12}M_{1/12}]O_2$, referred to as "M-doped". Optimal coordination of atoms within the transition metal layer were determined through structural relaxations, and are consistent with previously published work.[9] This configuration, shown in Figure 1a, creates four local TM environments surrounding oxygen ions, though this number is expanded with the incorporation of dopants and delithiation of the structure. Li-rich materials' initial charging plateau following transition metal redox is attributed to oxygen evolution.[7] As such, the state of delithiation selected for analysis of oxygen evolution is at a lithium concentration of 8/14, referred to as "delithiated". The relaxed structure on delithiation of the supercell was determined by analysing energies of all permutations of lithium removal. From this relaxed supercell, each oxygen atom was removed and a final calculation was performed. The oxygen vacancy formation energy, E^F_{Ov}, was calculated by

$$E^F_{Ov} = E\left(Li_{\frac{8}{12}}Ni_{\frac{3}{12}}Mn_{\frac{6}{12}}M_{\frac{1}{12}}O_{2-\frac{y}{12}}\right) + \frac{y}{24}E(O_2) - E\left(Li_{\frac{8}{12}}Ni_{\frac{3}{12}}Mn_{\frac{6}{12}}M_{\frac{1}{12}}O_2\right) - 1.36 \quad (1)$$

Results and Discussion

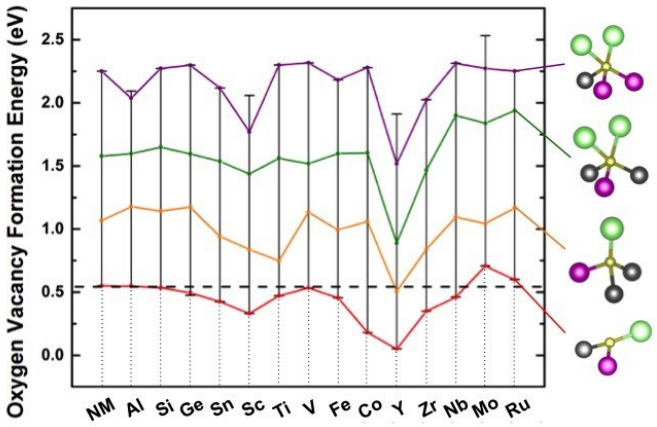

Figure 2: Distribution of oxygen vacancy formation energies, E_{Ov}^{F}, for each oxygen site for a full range of dopants. Representative bonding environments are indicated to reflect their relative E_{Ov}^{F}.

where the -1.36 eV correction factor is included to account for overbinding of GGA in molecular oxygen calculations. E_{Ov}^{F} was determined by removal of an oxygen ion from each oxygen site.[30] A similar process was performed for dopant incorporation, first determining the most stable site of the particularly dopant, delithiating, and extracting oxygen, further described in the Supplemental Information. Simulations with and without oxygen vacancies are relaxed and produce charge neutral supercells. Scaling was performed to ensure no spurious interactions between defects.

To briefly discuss current understanding of oxygen redox in Li-rich cathode materials, there are a few theories pertaining to the mechanism leading to oxygen oxidation: most prevalent theories are the formation of a peroxo-like species[4,31] and the formation of electron holes in certain oxygen bonding environments.[11,20] The notion of the peroxo-like formers has been experimentally viewed, but further computational and experimental work suggests that this phenomenon is limited to the case of 4d and 5d transition metal oxides, which may be phenomenologically viewed as having weaker localized bonding with oxygen, and allow more flexible bond angles with the subsequent formation of O-O bonds.[20,31,32] In the case of more traditional, commercially relevant materials consisting of 3d TM elements, TM-O bonds are viewed as more rigid. Both computation and experiment view the formation of peroxo-groups in these materials unlikely, and further evidence supports the presence of localized electron holes.[11,20] A similar rigidity is observed both in literature[20] and in our model calculations, for TM-O bonds. It is further noted that through the application of GGA+U, similar to the previously demonstrated use of hybrid functionals,[20] an increased partial density of states is observed near the Fermi energy for oxygen ions exhibiting a Li-O-Li bond (Supplemental Information). Despite the advantage of labile oxygen, as reflected in the initial charge capacity of lithium rich layered oxides, these easily oxidized anions also exhibit reduced bonding stability and are subject to removal. As such, calculation of E_{Ov}^{F} is critical in understanding anion stabilization.

From the calculated E_{Ov}^{F} results, a wide range of E_{Ov}^{F} is observed in the undoped, delithiated structure. To understand this E_{Ov}^{F} variation, it is first necessary to examine the relaxed structure of the undoped material, delithiated to the point where oxygen is experimentally observed to release from the lattice. The broad range of local atomic environments in the relaxed structure is seen to directly impact E_{Ov}^{F}, and is generally overlooked in simulated oxygen vacancy formation energy calculations. A critical feature of this relaxed structure is the formation of the lithium dumbbell or the migration of lithium ions to tetrahedral sites surrounding a TM-layer lithium vacancy, shown in Figure 1b.[9] Explicit representations of oxygen coordination environments with respect to the transition metal layer are provided in the Supplementary Information. A few trends are observed related to the variation in E_{Ov}^{F} in Figure 2. The lowest energy sites contain three critical environmental factors: (1) the presence of a Ni nearest neighbours generally results in a lower oxygen vacancy formation energy, due to reduced electrostatic repulsion between the oxygen vacancy (effectively a positive charge) and the less positive Ni cation;[13] (2) a minimized coordination with cations; and (3) subsequently occurs near a TM layer lithium vacancy and hence is in proximity to a tetrahedral lithium ion. The migration of lithium to the tetrahedral site creates a local environment loosely resembling a trigonal plane with a tetrahedral lithium, Ni ion, and Mn ion as vertices. Intuitively, this distorted trigonal planar environment does not well suit the orbital symmetry of oxygen ions, and the reduced bonding stability is evident through the reduced E_{Ov}^{F}.

Impact of Dopants on Oxygen Stability

Generally, a similar range in E_{Ov}^{F} is present in the doped and delithiated structures, though doping is seen to alter the distribution and magnitude of these energies. Al, Ti, Co and Mo were selected as representative dopants for further analysis, either showing little (Al, Ti) or notable changes (Co, Mo) in E_{Ov}^{F}. Of the simulated dopants, Mo and Ru are predicted to raise the

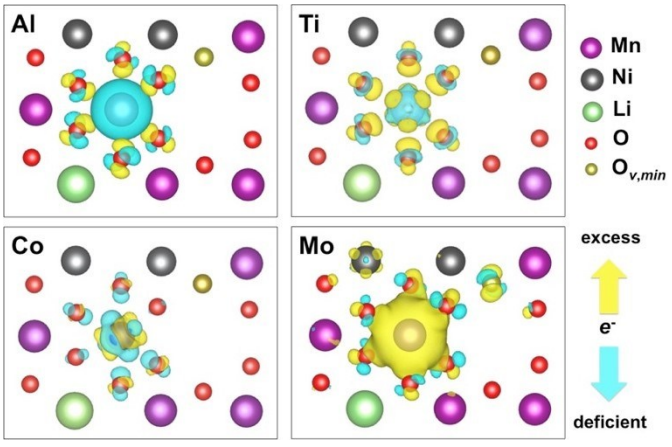

Figure 3: The difference in charge densities between undoped and doped structures (delithiated state; iso-surface of 0.01 electrons/Bohr^3) elucidates the alteration of electron distribution and bonding upon introduction of a dopant. Most notably, Mo-doping results in diffusely distributed electron excess, having a more notable change to the most susceptible bonding environment to oxygen loss. Ov,min (gold ion) denotes the minimum E_{Ov}^{F} site.

View Article Online
DOI: 10.1039/C8TA06206J

E^F_{Ov} of the lowest energy site for oxygen release. Despite Ru having shown an enhanced E^F_{Ov}, as well as interesting properties when used in lithium rich layered oxides, showing the formation of peroxo-like species on discharge,[4] the advantages of Ru doping are far outweighed by its cost, and hence will not be further discussed as a dopant in this

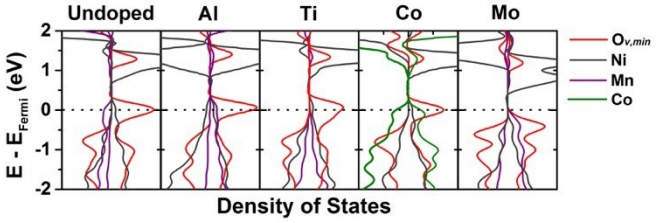

Figure 4: The partial density of states for the lowest E^F_{Ov} site and neighboring transition metals prior to oxygen removal. Analysis shows that Mo doping shifts the bonding states below the Fermi energy, and increases electron density below the Fermi energy, a potential sources of anion stabilization.

work. Similar to the undoped scenario, the lowest E^F_{Ov} is present at same local environment displaying the near-trigonal planar configuration. Al and Ti are further discussed for analytical comparison due to the calculated E^F_{Ov} being similar to that of the undoped material, and are of further interest due to their reduced cost and low toxicity, respectively. Last, Co was selected due to its predicted decrease in E^F_{Ov}, enhancing oxygen release, and its relevance in commercial cathode use. Co is also unique in that its predicted location is in proximity to the most volatile oxygen site (i.e., lowest E^F_{Ov}), which may further promote instability and oxygen loss.

To rationalize this predicted oxygen vacancy formation energy change, a site-dependent analysis of the delithiated charge density distribution and density of states (DOS) were performed to determine if the dopant affected the electronic behaviour of the cathode material. First, a Bader charge analysis was performed to observe trends in electron density with the incorporation of dopants, detailed in the Supplemental Information (Table S2). In previous oxygen vacancy formation studies,[23,25] oxygen sites with the lowest Bader charge and largest Bader charge difference between pristine and delithiated states are supposed to evolve most easily, and these sites are generally used for the E^F_{Ov} calculations. While this is the case for incorporated 3d transition metal dopants, Mo-doping shows a discrepancy between oxygen sites with maximum Bader charge difference and minimum E^F_{Ov}. Mo-doping also shows the highest net increase in charge density associated with oxygen sites. Last, a correlation is observed between average change in Bader charge upon delithiation and average E^F_{Ov}.

To better understand electron charge redistribution, charge density differences were calculated (Figure 3). For clarity, charge density differences between undoped and doped structures were calculated for the same dopant site, and in the case of Co will not reflect the exact bonding environment present in the minimum E^F_{Ov} value. However, for the intent of observing change in charge distribution, the simulation yields fundamentally applicable results. Intuitively, Al-doping presents a local charge deficiency, and the redistribution of charge on surrounding O 2p orbitals is a coulombic effect; this redistribution is local, and does not extend far beyond the immediate AlO_6 octahedron. Converse to Al, Ti-doping predicts an increased charge density on the oxygen in the surrounding TiO_6 octahedron; though similarly, the charge redistribution does not extend beyond the octahedrally coordinated oxygen. Variations in the charge density of Co- and Ti-doped structures reflect the modified bonding relative to the original Mn environment. The Co bonding results in a charge reduction on surrounding oxygen ions; as this Co is actually neighbouring the lowest E^F_{Ov} site, this oxygen ion will directly experience the reduced charge density and will more directly impact this site. Last, Mo shows the most significant charge redistribution, increasing charge density to local oxygen p orbitals. Interestingly this charge redistribution extends beyond the MoO_6 octahedron, increasing the charge density of the trigonal-planer-like oxygen site, a potential source of reduction of E^F_{Ov}.

E^F_{Ov} results are further described by the DOS calculations of the lowest E^F_{Ov} oxygen site and surrounding ions. Figure 4 shows that most dopants have little local impact on the DOS of this site, but for the case of the Mo-dopant a notable shift of the energy of local bonding orbitals below the Fermi energy is observed. This shift creates a barrier to charge transfer between bonding and antibonding orbitals for this particular oxygen ion, subsequently

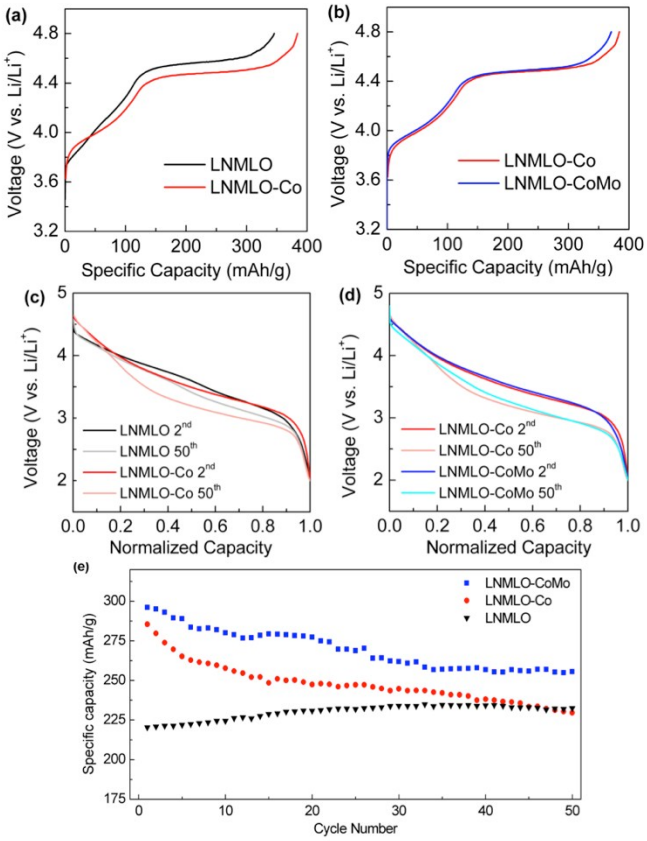

Figure 5: Cycling results of LNMLO, LNMLO-Co, and LNMLO-CoMo. Incorporation of Co (a) is shown to increase the initial charging plateau, where Mo-doping (b) reduces the plateau, suggesting reduced oxygen gas evolution. Mo-doping further shows reduced voltage decay (d) and improved capacity retention (e).

impeding the removal of oxygen from the oxygen sublattice.

Integration of the oxygen DOS between the Fermi energy and -1.5 eV shows a 27% increase in the electron density in the O 2p orbitals. This extra charge, due to the charge reconfiguration from Mo-doping, is the likely source of the relatively increased Fermi energy of the local bonding orbitals.

Table 1: A comparison of electrochemical performance parameters of LNMLO, LNMLO-Co and LNMLO-CoMo.

	Plateau length (mAh/g)	Average voltage (Cycle 50)	Specific capacity (Cycle 1/50, mAh/g)	Capacity retention (Cycle 50)
LNMLO	228.0	97.0%	220/232	105%
LNMLO-Co	266.9	93.6%	290/230	79.30%
LNMLO-CoMo	253.4	94.2%	297/256	86.50%

Experimental Observations

Guided by the E_{Ov}^{F} calculations, synthesis preceded with the dopants previously discussed in terms of calculation results: Co, Mo, Al, and Ti are incorporated into pristine Li-rich layered oxide cathode (LNMLO).

Co-doped LNMO (LNMLO-Co) was examined to observe the potential decrease in oxygen stability of the cathode material. It is known that Co readily forms a solid solution with LNMLO at large concentrations, allowing an amount of Co to be doped into LNMLO consistent with calculations. Shown in the works of Deng et al.[18] and Wang et al.,[21] electrochemical cycling can be partially described in terms of the calculated oxygen stability. The initial charging plateau in the cycling profile is attributed to both reversible anion redox and irreversible oxygen evolution. As predicted computationally, the Co-doped sample shows an extended initial charging plateau relative to the undoped material. As shown in Figure 5a, the plateau length of LNMLO is 228.0 mAh/g, while that of LNMLO-Co increases to 266.9 mAh/g. Cycling instability of the material is further presented in the form of the severe voltage decay after 50 cycles, shown in Figure 5c. The average voltage retention after 50 cycles decreases from 97% to 93.6% after Co doping. As compared in Figure 5e, LNMLO-Co delivers significantly improved discharge capacities in the initial several cycles but drops sharply. The LNMLO-Co shows a first discharge capacity of 290 mAh/g, while that of pristine LNMLO only delivers 220 mAh/g reversible capacity. This increased capacity in LNMLO-Co may be due to the increased activation of redox-active oxygen. After 50 cycles, the capacity of LNMLO-Co only maintains 79.3% of initial capacity, 230 mAh/g. Yet, the capacity of LNMLO slightly increases to 232 mAh/g. The experimental observations are in complete agreement with the computational prediction that Co doping leads to decreased oxygen stability, resulting in increased irreversible oxygen gas evolution.

Aiming to provide insight for practical application, obtaining high energy density while maintaining excellent cycling stability, Mo doping is performed on LNMLO-Co material (LNMLO-CoMo). 1% of Mo was doped into bulk of LNMLO-Co, as will be evident. Doping of 3% of Mo into LNMLO-Co structure was also attempted; however, impurity peaks appear (Figure S8), consistent with previous literature. 1% is likely near the maximum amount of doping into the structure, due to the large ionic radius of Mo.[33] The first charging curve of LNMLO-CoMo (Figure 5b) shows a reduced initial charging plateau (253.4 mAh/g) compared with LNMLO-Co (266.9 mAh/g). This indicates, conversely to the Co material, a reduction in electron charge transfer from oxygen, which would otherwise accompany the irreversible oxygen loss from the lattice. The material also shows moderately less voltage decay after 50 cycles (Figure 5d). The average voltage retention improves by 0.6% with Mo doping. Last, and most notably, the specific capacity and cycling stability are greatly improved. As shown in Figure 5e, LNMLO-CoMo delivers a high reversible capacity of 297 mAh/g. After 50 cycles, the capacity remains 256 mAh/g with retention of 86.5%. Note that the coulombic efficiency can be further improved upon application of surface treatment,[14] though in this work we focus on the bulk doping only. A detailed electrochemical performance comparison of the three samples is shown in Table 1. EIS measurements are also carried out to understand the variation in electrochemical behaviour of LNMLO-Co and LNMLO-CoMo (Figure S3). In the pristine state, both compositions are dominated by charge transfer resistance, and after 30 cycles an SEI component is observed. Though the Mo-doped sample shows reduced charge transfer resistance

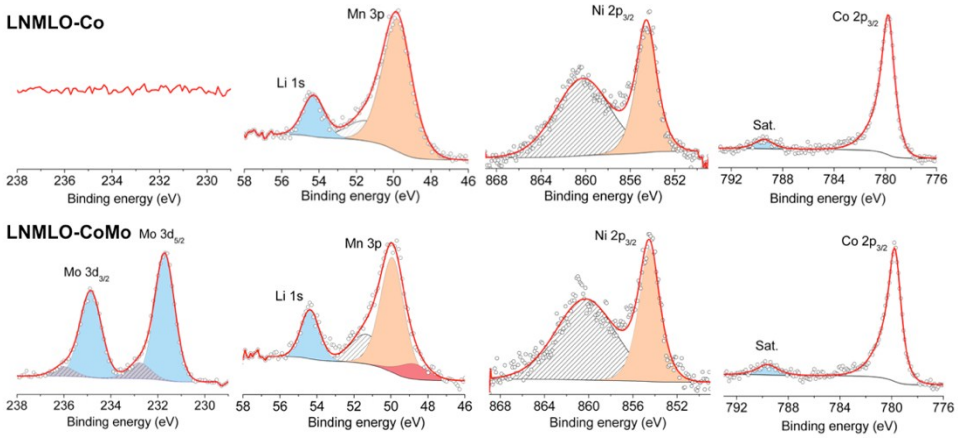

Figure 6: XPS of LNMLO-Co and LNMLO-CoMo show that Mo took the predicted Mo^{5+} valence. Results further show a portion of the Mn is reduced from Mn^{4+} to Mn^{3+} with the incorporation of Mo.

View Article Online
DOI: 10.1039/C8TA06296J

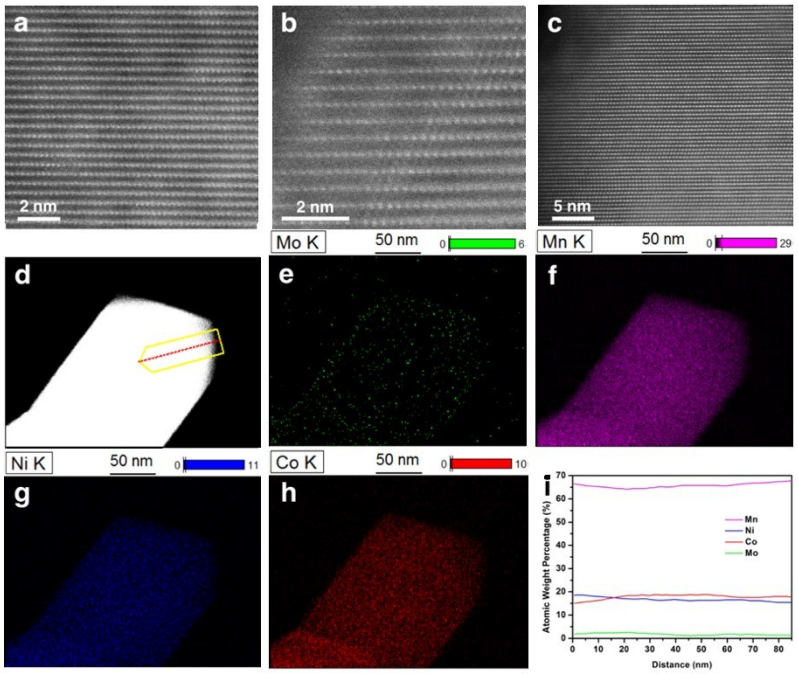

Figure 7: HAADF images of pristine LRLO-CoMo (a) bulk and (b) surface, and (c) pristine LRLO-Co, showing both surface and bulk. STEM/EDS mapping of a primary particle shows a uniform distribution of all constituents (e-h). Quantitative analysis (i) was attained by an EDS line-scan, acquired along the red line in the direction of the yellow arrow in (d).

before and after cycling, and much smaller SEI component after 30 cycles, indicating improved electron transfer and lithium ion diffusion with only 1% incorporation of Mo. The above results clearly demonstrate the positive effect of Mo doping on electrochemical performance.

The incorporation of Mo into the structure was verified by XRD, XPS, STEM, and EDS: (1) Figure S6 compares XRD and Rietveld refinement results of LNMLO, LNMLO-Co and LNMLO-CoMo materials. The lattice parameter variation trend of the three materials is shown in Figure S7. Co^{3+} (0.545 Å) doping leads to shrinking of *a*- and *c*-lattice parameters compared with pristine LNMLO. A slight a-lattice expansion is caused by Mo^{5+} (0.61 Å) substitution into the structure, also noting that Mo^{5+} doping causes significant expansion of the c-lattice parameter due to the increased Mo-O bond length. The increased c-lattice parameter facilitates Li^+ diffusion, explaining in part the increment of capacity in LNMLO-CoMo material. (2) Figure 6 compares the XPS analysis of LNMLO-Co and LNMLO-CoMo samples. Results of the XPS suggest that most of the Mo dopant takes the Mo^{5+} oxidation state in the pristine state. Specifically, the two peaks at binding energies of 231.7 eV and 234.8 eV are attributed to Mo^{5+}. Weak shoulders at higher binding energy of 232.8 eV and 236 eV indicate a small amount of Mo^{6+}.[34] Oxidation states of TM's are predicted using magnetization data from DFT calculations (Table S3), and calculate Mo in the pristine state to have a +5 charge. This dopant is predicted to be oxidized to Mo^{6+} on the first delithiation, not explored in this work. Oxidation states of Ni show no change, as the peak at 854.5 eV does not shift after Mo doping. Mn appears to be slightly reduced, again consistent with computation results. The predicted mixed valence of Mn may enhance the conductivity of the material, partially explaining the increased specific capacity.[33] Co is slightly reduced after Mo doping, as the satellite peak area increases from 6.84% to 8.99% after doping.[35] (3) The most convincing evidence comes in the form of aberration corrected high angle annular dark field (HAADF) STEM images of pristine particles (Figure 7). Incorporation of Mo is clearly correlated with an increase in lattice strain, as evident by the contrast non-uniformity in the doped particle (Figure 7a). Transition metal migration to the lithium layer was observed near the particle sub-surface, likely correlated with the increased strain (Figure 7b).[8] HAADF image of the pristine LNMLO-Co shows a typical structure with well layered properties in the bulk of the pristine material extended to the surface (Figure 7c). (4) EDS mapping of a primary particle of LNMLO-CoMo acquired in STEM shows a uniform distribution of all transition metal constituents (Figures 7e-h). Quantitative data acquired by line scan (Figure 7d) show the transition metals in the appropriate concentration from synthesis, and further illustrate the uniform distribution through the surface and bulk (Figure 7i). Mo distribution homogeneity was also observed by EDS of cross-sectioned secondary particles within a dual-beam FIB/SEM, as shown in Figure S9. It is noted that Mo-doping has indeed been explored for lithium rich layered oxides Li_2MnO_3,[36] $Li[Li_{0.2}Ni_{0.2}Mn_{0.6}]O_2$,[33] and $Li[Li_{0.2}Mn_{0.54}Ni_{0.13}Co_{0.13}]O_2$,[37,38] and in the case of Li_2MnO_3, Mo^{5+} was observed by X-ray absorption spectroscopy. Though again, little to no emphasis was placed on the stabilization of oxygen within the lattice in these prior works.

We further incorporated Al and Ti dopants into the pristine LRLO structure, as discussed in the Supplemental Information, showing results commensurate with calculated prediction, with little to no change is observed in the length of the high voltage oxygen-redox plateau.

Experimentally, a variety of dopants, including Al, Ti, Co and Mo, were selected to evaluate the impact on initial charge plateau, voltage fade, and capacity loss, and results are presented in the context of ab initio calculations. The observed electrochemical performance suggests that Al and Ti doping shows little impact on oxygen activities, having no effect on the width of the initial charging plateau; Co leads to decreased oxygen stability, increasing the width of the plateau; incorporation of Mo can mitigate oxygen loss from the lattice to some extent—consistent with E^F_{Ov} calculations. In this work, both theoretical and experimental findings show Mo-doped LNMLO shows the highest specific capacity and improved cycling stability.

Conclusions

Oxygen vacancy formation energies, E^F_{Ov}, were calculated for a wide range of dopants using ab initio calculations. The range of calculated E^F_{Ov} were shown to be strongly dependent on local environment, both compositionally and structurally. The source of E^F_{Ov} change between dopants was attributed to the charge density modification and subsequent change in band structure, increasing the E^F_{Ov} in the case of a Mo dopant. These calculated E^F_{Ov} values guided experimental doping, showing results in line with computational prediction. Al- and Ti-doped materials showed little change to the initial charging plateaus, consistent with the predicted E^F_{Ov}, where Co-doping showed an increase in the plateau width, indicating exaggerated oxygen loss from the lattice. Mo-doping experiments shows improved cycling stability through reduced voltage decay, suggesting oxygen is stabilized by the incorporation of Mo. Experiments show the presence of a majority of Mo^{5+} ions, as predicted. When considering the nature of oxygen activity within cathode material, it is clear that the formation of molecular oxygen in the bulk of the material accounts for the majority of this irreversible capacity loss. As such, methods of mitigating must extend beyond surface modification. Calculation results show that doping of particular elements (Mo and Ru) work to reduce the degree of oxygen loss from the lattice, while leaving the oxygen available for redox. However, the degree of dopant incorporation is limited by solubility of the dopant in the structure. This work validates cationic substitution as a fundamental method of improving capacity retention of lithium rich layered oxide cathodes, and should be combined with advanced surface modification to result in improved high capacity cathodes. This work further demonstrates the application of density functional theory towards the rational design of cathode materials, streamlining the design process and speeding the optimization of these materials.

Conflicts of interest

There are no conflicts to declare.

Acknowledgements

This collaborative work was supported by the US Air Force Office of Scientific Research and the Asian Office of Aerospace Research and Development, project number 15IOA110. M.Z., H.L., D.M.D., X.W., J.Z.L. and Y.S.M. acknowledge the partial funding from the Assistant Secretary for Energy Efficiency and Renewable Energy, Office of Vehicle Technologies of the U.S. Department of Energy (DOE) under Contract No. DE-AC02-05CH11231, Subcontract No. 7073923, under the Advanced Battery Materials Research (BMR) Program for sponsoring the advanced characterization efforts in this work. This work used the Extreme Science and Engineering Discovery Environment (XSEDE), which is supported by National Science Foundation grant number ACI-1548562. HAADF images for LNMLO-CoMo materials were carried out through a user project (2017- 119) supported by ORNL's Center for Nanophase Materials Sciences (CNMS), which is a DOE Office of Science User Facility. HAADF image for LNMLO-Co materials was collected from our previous work[14] at Brookhaven National Laboratory supported by the U.S. DOE, Office of Basic Energy Science. STEM/EDS and XPS was performed at the UC Irvine Materials Research Institute (IMRI) using instrumentation funded in part by the National Science Foundation Major Research Instrumentation Program under grant no. CHE-1338173. FIB/EDS were performed in part at the San Diego Nanotechnology Infrastructure (SDNI), a member of the National Nanotechnology Coordinated Infrastructure, which is supported by the National Science Foundation (grant ECCS-1542148). The authors thank M. Olguin for fruitful discussion.

Notes and references

1 J. B. Goodenough and Y. Kim, *Chem. Mater.*, 2010, **22**, 587–603.
2 J.-M. Tarascon and M. Armand, *Nature*, 2001, **414**, 359–367.
3 H. Yu and H. Zhou, *J Phys Chem Lett*, 2013, **4**, 1268–1280.
4 M. Sathiya, G. Rousse, K. Ramesha, C. P. Laisa, H. Vezin, M. T. Sougrati, M.-L. Doublet, D. Foix, D. Gonbeau, W. Walker, a S. Prakash, M. Ben Hassine, L. Dupont and J.-M. Tarascon, *Nat. Mater.*, 2013, **12**, 827–835.
5 K. Luo, M. R. Roberts, N. Guerrini, N. Tapia-Ruiz, R. Hao, F. Massel, D. M. Pickup, S. Ramos, Y. S. Liu, J. Guo, A. V Chadwick, L. C. Duda and P. G. Bruce, *J. Am. Chem. Soc.*, 2016, **138**, 11211–11218.
6 G. Assat and J. M. Tarascon, *Nat. Energy*, 2018, **3**, 373–386.
7 S. Hy, H. Liu, D. Qian, M. Zhang, B. J. Hwang and Y. S. Meng, *Energy Environ. Sci.*, 2016, **9**, 1931–1954.
8 C. R. Fell, D. Qian, K. J. Carroll, M. Chi, J. L. Jones and Y. S. Meng, *Chem. Mater.*, 2013, **25**, 1621–1629.
9 B. Xu, C. R. Fell, M. Chi and Y. S. Meng, *Energy Environ. Sci.*, 2011, **4**, 2223–2233.
10 A. R. Armstrong, M. Holzapfel, P. Novák, C. S. Johnson, S. H. Kang, M. M. Thackeray and P. G. Bruce, *J. Am. Chem. Soc.*, 2006, **128**, 8694–8698.
11 K. Luo, M. R. Roberts, R. Hao, N. Guerrini, D. M. Pickup, Y.-S. Liu, K. Edström, J. Guo, A. V. Chadwick, L. C. Duda and P. G. Bruce, *Nat. Chem.*, 2016, **8**, 684–691.
12 H. Liu, Y. Chen, S. Hy, K. An, S. Venkatachalam, D. Qian, M. Zhang and Y. S. Meng, *Adv. Energy Mater.*, 2016, n/a-n/a.
13 D. Qian, B. Xu, M. Chi and Y. S. Meng, *Phys. Chem. Chem. Phys.*,

View Article Online
DOI: 10.1039/C8TA06296J

2014, **16**, 14665–14668.
14 B. Qiu, M. Zhang, L. Wu, J. Wang, Y. Xia, D. Qian, H. Liu, S. Hy, Y. Chen, K. An, Y. Zhu, Z. Liu and Y. S. Meng, *Nat. Commun.*, 2016, **7**, 12108.
15 H. Liu, J. Huang, D. Qian, S. Hy, C. Fang, J. Luo and Y. S. Meng, *J. Electrochem. Soc.*, 2016, **163**, A971–A973.
16 G. R. Li, X. Feng, Y. Ding, S. H. Ye and X. P. Gao, *Electrochim. Acta*, 2012, **78**, 308–315.
17 K. Luo, M. R. Roberts, R. Hao, N. Guerrini, E. Liberti, C. S. Allen, A. I. Kirkland and P. G. Bruce, *Nano Lett.*, 2016, **16**, 7503–7508.
18 Z. Q. Deng and A. Manthiram, *J. Phys. Chem. C*, 2011, **115**, 7097–7103.
19 E. McCalla, M. T. Sougrati, G. Rousse, E. J. Berg, A. Abakumov, N. Recham, K. Ramesha, M. Sathiya, R. Dominko, G. Van Tendeloo, P. Novák and J. M. Tarascon, *J. Am. Chem. Soc.*, 2015, **137**, 4804–4814.
20 D. Seo, J. Lee, A. Urban, R. Malik, S. Kang and G. Ceder, *Nat. Chem.*, 2016, **8**, 692–697.
21 C.-C. Wang and A. Manthiram, *J. Mater. Chem. A*, 2013, **1**, 10209–10217.
22 P. Xiao, Z. Q. Deng, A. Manthiram and G. Henkelman, *J. Phys. Chem. C*, 2012, **116**, 23201–23204.
23 Y. Gao, X. Wang, J. Ma, Z. Wang and L. Chen, *Chem. Mater.*, 2015, **27**, 3456–3461.
24 F. Kong, R. C. Longo, M.-S. Park, J. Yoon, D.-H. Yeon, J.-H. Park, W.-H. Wang, S. Kc, S.-G. Doo and K. Cho, *J. Mater. Chem. A*, 2015, **3**, 8489–8500.
25 Y. Gao, J. Ma, X. Wang, X. Lu, Y. Bai, Z. Wang and L. Chen, *J. Mater. Chem. A*, 2014, **2**, 4811–4818.
26 J. Li, C. Zhan, J. Lu, Y. Yuan, R. Shahbazian-Yassar, X. Qiu and K. Amine, *ACS Appl. Mater. Interfaces*, 2015, **7**, 16040–16045.
27 J. Liu, S. Wang, Z. Ding, R. Zhou, Q. Xia, J. Zhang, L. Chen, W. Wei and P. Wang, *ACS Appl. Mater. Interfaces*, 2016, **8**, 18008–18017.
28 B. Li, H. Yan, Y. Zuo and D. Xia, *Chem. Mater.*, 2017, **29**, 2811–2818.
29 A. I. Liechtenstein, V. I. Anisimov and J. Zaanen, *Phys. Rev. B*, 1995, **52**, R5467.
30 L. Wang, T. Maxisch and G. Ceder, *Phys. Rev. B*, 2006, **73**, 195107.
31 E. McCalla, A. M. Abakumov, M. Saubanère, D. Foix, E. J. Berg, G. Rousse, M.-L. Doublet, D. Gonbeau, P. Novák, G. Van Tendeloo, R. Dominko and J.-M. Tarascon, *Science*, 2015, **350**, 1516–1521.
32 M. Saubanère, E. McCalla, J.-M. Tarascon and M.-L. Doublet, *Energy Environ. Sci.*, 2016, **9**, 984–991.
33 Y. Zang, C.-X. Ding, X.-C. Wang, Z.-Y. Wen and C.-H. Chen, *Electrochim. Acta*, 2015, **168**, 234–239.
34 X. Deng, S. Y. Quek, M. M. Biener, J. Biener, D. H. Kang, R. Schalek, E. Kaxiras, C. M. Firend, X. Deng, S. Y. Quek, M. M. Biener, J. Biener, D. H. Kang, R. Schalek, E. Kaxiras and C. M. Friend, *Surf. Sci.*, 2007, **602**, 1166–1174.
35 S. Verdier, L. El Ouatani, R. Dedryvère, F. Bonhomme, P. Biensan and D. Gonbeau, *J. Electrochem. Soc.*, 2007, **154**, A1088.
36 J. Ma, Y.-N. Zhou, Y. Gao, Q. Kong, Z. Wang, X.-Q. Yang and L. Chen, *Chem. - A Eur. J.*, 2014, **20**, 8723–8730.
37 X. Yuan, Q. Xu, X. Liu, W. Shen, H. Liu and Y. Xia, *Electrochim. Acta*, 2016, **207**, 120–129.
38 J. Du, Z. Shan, K. Zhu, X. Liu, J. Tian and H. Du, *J. Solid State Electrochem.*, 2015, **19**, 1037–1044.